



HAL
open science

New Features and Uncovered Benefits of Polycrystalline Magnetite as Reusable Catalyst in Reductive Chemical Conversion

Sungjun Bae, Suji Gim, Hyungjun Kim, Vincent Dorcet, Mathieu Pasturel, Jean-Marc Greneche, Gopala Krishna Darbha, Khalil Hanna

► **To cite this version:**

Sungjun Bae, Suji Gim, Hyungjun Kim, Vincent Dorcet, Mathieu Pasturel, et al.. New Features and Uncovered Benefits of Polycrystalline Magnetite as Reusable Catalyst in Reductive Chemical Conversion. *Journal of Physical Chemistry C*, 2017, 121 (45), pp.25195-25205. 10.1021/acs.jpcc.7b08178 . hal-01659405

HAL Id: hal-01659405

<https://univ-rennes.hal.science/hal-01659405>

Submitted on 11 Jan 2018

HAL is a multi-disciplinary open access archive for the deposit and dissemination of scientific research documents, whether they are published or not. The documents may come from teaching and research institutions in France or abroad, or from public or private research centers.

L'archive ouverte pluridisciplinaire **HAL**, est destinée au dépôt et à la diffusion de documents scientifiques de niveau recherche, publiés ou non, émanant des établissements d'enseignement et de recherche français ou étrangers, des laboratoires publics ou privés.

New Features and Uncovered Benefits of Polycrystalline Magnetite as Reusable Catalysts in Reductive Chemical Conversion

Sungjun Bae,^{*a} Suji Gim,^b Hyungjun Kim,^b Vincent Dorcet,^c Mathieu Pasturel,^c Jean-Marc
Grenèche,^d Gopala Krishna Darbha,^{e,f} Khalil Hanna^{*g}

^aDepartment of Environmental Engineering, Konkuk University, 120 Neungdong-ro,
Gwangjin-gu, Seoul 05029, Republic of Korea

^bGraduate School of Energy, Environment, Water, and Sustainability (EEWS), Korea
Advanced Institute of Science and Technology, 291 Daehak-ro, Yuseong-Gu, Daejeon 305-
701, Republic of Korea

^cInstitut des Sciences Chimiques de Rennes, UMR CNRS 6226, 263 avenue Général Leclerc,
35042 Rennes Cedex 7, France

^dInstitut des Molécules et Matériaux du Mans, UMR CNRS 6283, Université du Maine,
72085 Le Mans Cedex 9, France

^eNational Institute of Technology – Andhra Pradesh, Tadepalligudem, Andhra Pradesh,
534101, India

^fInstitut für Nukleare Entsorgung (INE), Karlsruhe Institute of Technology (KIT), P.O. Box
3640, 76021 Karlsruhe, Germany

^gÉcole Nationale Supérieure de Chimie de Rennes, UMR CNRS 6226, 11 Allée de Beaulieu,
35708 Rennes Cedex 7, France

*Co-corresponding authors: Tel.: +82 2 450 3904, +33 2 23 23 80 27

E-mail address: bsj1003@konkuk.ac.kr (S. Bae), khalil.hanna@ensc-rennes.fr (K. Hanna)

Journal of Physical Chemistry C

September, 2017

Abstract

Magnetite is one of the most well characterized and facilitated iron oxide in a variety of research and industrial fields. Especially, its easy separation by magnetism has attracted a great attention to use as a support material for various noble metallic catalysts. Here, we report for the first time that bare polycrystalline magnetite can show a remarkable catalytic activity toward *p*-nitrophenol reduction by sodium borohydride, while other three single-crystal magnetite exhibit little effect on the catalysis. Electron and atomic force microscopies and Mössbauer spectroscopy showed that elemental Fe nanoparticles were formed on the surface of polycrystalline magnetite. Density functional theory calculation further elucidated that the Fe atom exposed at the high-index magnetite surface develops a significant Fe-BH₃ interaction and its leaching-out process can be substantially promoted. Surprisingly, recycling tests showed that this great activity could be fully preserved up to 10 reaction cycles, in contrast to the other noble metal-based catalysts showing a decrease in the catalytic activity as the reaction cycle increased.

Introduction

Catalytic reactions have been extensively applied to over 90% of all chemical manufacturing, contributing thus at around 35% of the world's gross domestic product.¹ Especially, homogenous catalysts are commonly used for production of fine chemicals and pharmaceuticals. However, some drawbacks limit the reuse of catalysts due to contamination with final products and formation of metal complexes.² In contrast, heterogeneous catalysts have attracted much attention in the catalysis processes for the past few decades because of their advantages such as well-defined structural materials, easy handling, and simple solid-liquid separation.^{1,2} Heterogeneous catalysts produce around 95% of bulk chemicals and 3–5% of fine chemicals (accounting 20% of profit).²

In heterogeneous catalysis, a variety of noble metals (e.g., Au, Pt, Pd, and Ag) are widely used for effective catalytic reactions and usually immobilized on other supports (e.g., carbon materials, polymers, and metal oxides) to prevent the loss of the noble metals after the catalytic reactions.^{3–9} Among the support materials, many types of iron oxides such as FeO (wüstite), γ -Fe³⁺₂O₃ (maghemite), α -Fe³⁺₂O₃ (hematite) have been successfully used to develop efficient, low-cost, and recyclable supported catalysts for organic and inorganic transformation for the past few decades.^{10–13} In particular, magnetite (Fe²⁺₁Fe³⁺₂O₄), a face-centered cubic unit cell containing the Fe³⁺ ion in tetrahedral sites and both Fe³⁺ and Fe²⁺ ions in octahedral sites with 32 O²⁻ ions, has shown an outstanding applicability not only in solid-supported catalysis but also in other-disciplinary research (e.g., semiconductor, magnetic resonance imaging, pigment, biomedicine, drug delivery, and environmental remediation)^{2,14,15} due to its unique magnetic properties and easy manipulation for control of morphologies, particle size, and Fe²⁺/Fe³⁺ stoichiometry.^{12,15–19} However, determination of magnetite compositions which is highly sensitive to the preparation conditions is not a trivial task, particularly for nanoscale particles with a higher surface-to-volume ratio.²⁰ Indeed, magnetite compositions range, without modification of crystal structure, from that of

1
2
3 stoichiometric Fe_3O_4 , with 8 Fe^{3+} ions in tetrahedral and 8 $\text{Fe}^{2+} + 8 \text{Fe}^{3+}$ ions in octahedral
4
5 sites, to that of maghemite $\gamma\text{-Fe}^{\text{III}}_2\text{O}_3$ (considered as an extreme example of a non-
6
7 stoichiometric magnetite) with only Fe^{3+} ions in both tetrahedral and octahedral sites.²¹
8

9
10 Sodium borohydride (NaBH_4) induced *p*-nitrophenol (*p*-NP) reduction to *p*-
11
12 aminophenol (*p*-AP), is perhaps the most widely used catalytic model reactions to check the
13
14 catalytic activity of the heterogeneous catalysts.²²⁻²⁹ Indeed, a large number of studies has
15
16 struggled to develop novel magnetite-supported catalysts using different materials such as Ag,
17
18 Au, Ag-SiO₂, Cu-graphene, SiO₂-CeO₂, Co-Se, and Pt-Pd and proved their remarkable
19
20 catalytic activity for *p*-NP reduction.^{5,6,8,23-28} In the previously reported studies, control
21
22 experiments using bare magnetite (< 300 nm) have normally shown little effect on the
23
24 catalytic activity, indicating that magnetite itself does not possess any catalytic activity but
25
26 only acts as a support during the catalysis.^{5,6,28} On the other hand, our recent findings showed
27
28 that magnetite can provide the reactive surface for *p*-NP reduction in NaBH_4 induced catalytic
29
30 reaction³⁰ which is contrary to those known already. This may be because the catalytic
31
32 activity of magnetite in NaBH_4 induced catalytic reaction may be dependent on the physical
33
34 and chemical properties of bare magnetite. However, a limited knowledge has been provided
35
36 for understanding of interaction between different type of magnetite and NaBH_4 and its
37
38 potential application to reductive transformation of organic compounds to date.
39
40
41
42

43 Here, we report for the first time that important reduction of *p*-NP using bare magnetite
44
45 without precious noble metals can be achieved, but this reactivity is strongly dependent on
46
47 surface and structure properties of magnetite. The main objectives of this study were to (i)
48
49 examine the reaction of four different magnetite during the NaBH_4 induced *p*-NP reduction,
50
51 (ii) investigate the catalytic reaction mechanism at molecular level supporting by a variety of
52
53 surface analysis and theoretical study (i.e., density functional theory (DFT) calculation), and
54
55 (iii) find out a feasibility to use magnetite as an effective, durable, economical, and
56
57
58
59
60

manageable catalytic material without using expensive noble metals widely used in heterogeneous catalysis.

Experimental Methods

Materials and chemicals. Four different sizes of lab-synthesized and commercial magnetite were prepared for this study. Magnetite 1 (M1, 10–20 nm) and 2 (M2, 50–200 nm) were differently synthesized by Fe(II) induced transformation from ferrihydrite³¹ and co-precipitation method using Fe(II) and Fe(III) solutions. Magnetite 3 (M3, 100–500 nm) and 4 (M4, 100 nm–10 μ m) were purchased from Aldrich Chemical Co. and Prolabo Co., respectively. Chemicals used in the experiment were ferric chloride (98%, Sigma), ferrous sulfate (99%, Sigma), *p*-NP (>99%, Sigma), *p*-aminophenol (*p*-AP) (>98%, Sigma), sodium hydroxide (95%), and sodium borohydride (99%, Sigma). Acetonitrile (HPLC grade, J.T.Baker, USA) and acetic acid (99.7%, ACROS) were used for mobile phase of high performance liquid chromatography (HPLC). All experiments were prepared using deionized water (DIW), prepared using ultra-pure water (18M Ω ·cm).

Catalytic reduction of *p*-NP by magnetite. The reduction of *p*-NP by four different magnetite samples was carried out in the presence of 100 mM NaBH₄. An exact amount of magnetite (3 mg) was added into a quartz cuvette containing 2.7 mL of the NaBH₄ solution (100 mM) and 0.3 mL of *p*-NP (1 mM) in NaBH₄ solution (100 mM) to initiate the reduction of *p*-NP. The total volume of reaction mixture was thus 3 mL with initial concentrations of 1 g/L magnetite and 0.1 mM *p*-NP, respectively. The concentration of *p*-NP was measured at 400 nm wavelength by UV-vis spectrophotometer (CARY 50 probe, Varian). To investigate the effect of NaBH₄ concentration on the catalytic activity of M4, other four different concentrations of NaBH₄ (10, 25, 50, and 200 mM) were used for the reduction of *p*-NP. A recycling test (10 times) was also conducted using M4. After finishing the reduction of *p*-NP,

1
2
3 magnetite used was magnetically collected at the bottom of the cuvette by removal of aqueous
4
5 solution, then washed three times with DIW to remove the residual *p*-AP and finally, NaBH₄
6
7 (2.7 mL) and *p*-NP (0.3 mL) were added into the quartz cuvette for recycling test.
8
9

10
11 **HPLC analysis and Fe and H₂ measurements.** The final concentrations of *p*-NP and *p*-AP
12
13 in aqueous solution were confirmed by HPLC (Waters) equipped with a C18 packed column
14
15 (Waters) and UV detector. An exact amount of aqueous sample (2.0 mL) was collected by a
16
17 sterilized disposable syringe after finishing the catalysis experiment. Then, the sample was
18
19 filtered through a 0.2- μ m membrane filter and 1 mL of the filtered sample was transferred
20
21 into HPLC auto-sampler vials. The concentrations of *p*-NP and *p*-AP were quantified at
22
23 wavelengths of 317 and 273 nm at a flow rate of 1.0 mL min⁻¹. A mixture of 49.5% DIW,
24
25 49.5% acetonitrile, and 1% CH₃COOH was used for the mobile phase.
26
27
28

29
30 Fe²⁺ and Fe³⁺ contents for each magnetite were measured by the ferrozine method using
31
32 an UV-vis spectrophotometer. Magnetite was fully dissolved in 6 M HCl deaerated by N₂,
33
34 then the amounts of Fe²⁺ were measured at the wavelength of 562 nm.³² The total Fe was also
35
36 measured by adding 10% hydroxylamine solution. Fe(III) concentration was calculated by
37
38 subtracting Fe(II) concentration from the total Fe concentration. The concentration of
39
40 dissolved Fe²⁺ was not significant in membrane-filtered samples, indicating that the Fe
41
42 dissolution from magnetite can be considered as negligible in this study.
43
44

45
46 The contents of H₂, O₂, and N₂ in the magnetite-NaBH₄ suspension were measured by a
47
48 gas chromatograph (GC, Shimadzu 8A) equipped with a thermal conductivity detector and a
49
50 2-m stainless column packed with Porapak Q (50/80 mesh). An exact amount of magnetite (3
51
52 mg) was transferred to serum bottles (total volume: 21.9 mL) containing 3 mL of NaBH₄ (100
53
54 mM). Headspace sampling was conducted and 1 mL of gas samples were introduced into the
55
56 injection port by a gastight syringe. We measured the amount of each gas in head space and
57
58 re-calculated the percentage value of each gas in total amount. The operational temperatures
59
60

1
2
3 of the injection port, the oven and the detector were 100, 70 and 100°C, respectively. Helium
4
5 was used as the carrier gas at a flow rate of 30 ml·min⁻¹
6
7

8
9 **Surface characterization.** The morphological change of magnetite was identified by
10 transmission electron microscopy (TEM) using JEM-2100 (JEOL) microscope working at 200
11 KV equipped with a scanning module and with an energy dispersive X-ray detector (Oxford)
12 for elemental mapping analysis and by scanning electron microscopy (SEM) using JSM-
13 7100F (JEOL). The samples before and after the reaction with NaBH₄ were transferred into an
14 anaerobic chamber (JACOMEX) to avoid the oxidation of magnetite by O₂ and washed twice
15 with deaerated ethanol. The magnetite suspensions in ethanol phase were stored in the
16 anaerobic chamber prior to their use for electron microscopy. For TEM analyses, one droplet
17 of the diluted magnetite suspension was put on Cu grids. For SEM analysis, the magnetite
18 suspension was deposited on a carbon tape and the samples analyzed by SEM.
19
20
21
22
23
24
25
26
27
28
29
30
31

32 The quantity of iron phases, unit-cell lengths, and average crystallite size for each
33 magnetite before and after the reaction with NaBH₄ were obtained by Le Bail or Rietveld
34 refinement of X-ray diffraction (XRD) patterns (D8 Advance, BRUKER). The magnetite
35 suspensions prepared in ethanol phase were used for XRD analysis. The suspensions were
36 transferred to XRD holder and dried for 1 h in the anaerobic chamber. The dried samples were
37 treated with 1:1 (V:V) glycerol solution to avoid the oxidation of magnetite samples during
38 the XRD measurement.^{29,33} XRD patterns were collected in a modified Bragg-Brentano θ - 2θ
39 geometry goniometer working with a Ge(111) monochromatized Cu K α 1 radiation (λ =
40 1.5406 Å) and scanned between 10° and 80° with steps of 0.02° and integration time of 179 s
41 step⁻¹. The diffractometer is equipped with a LynxEye fast detector enabling the removal of
42 iron fluorescence signal. The iron phases were identified by matching XRD patterns of each
43 sample with the Joint Committee on Powder Diffraction Standards diffraction data files
44 (JADE 9, Materials Data, Inc.). Le Bail and Rietveld refinements were performed using the
45
46
47
48
49
50
51
52
53
54
55
56
57
58
59
60

1
2
3 Fullprof program.³⁴ The crystallite size was determined from the previous refinements by
4 fitting the lorentzian broadening of the diffraction peaks using a Thompson-Cox-Hastings
5 peak profile function and taking into account the instrumental resolution function.³⁵
6
7

8
9 Atomic force microscopy (AFM) is a powerful technique to characterize the
10 morphology of nanoparticles at high resolution (~nm scale). Herein, AFM (Digital
11 Instruments Dimension 3100 equipped with nanoscope IV controller) was applied to study the
12 change in topography of M4 in the absence and presence of NaBH₄ (100 mM). A droplet of
13 magnetite suspension was placed on a freshly cleaved biotite substrate and allowed to dry
14 before measurement. The experiments were performed in contact mode with a cantilever of
15 spring constant 0.35 N/m (SNL-10, Bruker AFM probes). The obtained images are processed
16 in Scanning Probe Image Processing (SPIP) software (Image metrology) applying the line
17 profile analysis.
18
19
20
21
22
23
24
25
26
27
28

29 ⁵⁷Fe Mössbauer spectra were obtained at 300 and 77 K using a conventional constant
30 acceleration transmission spectrometer with a ⁵⁷Co(Rh) source. The samples resulting from
31 drying solutions are containing about 5 mg/cm². They were located in a bath cryostat for low
32 temperature measurements. The spectra were fitted by means of the MOSFIT program
33 involving quadrupolar doublets and/or magnetic sextets, both composed of Lorentzian lines.
34 The relative proportions of these Fe species are estimated from the corresponding absorption
35 areas, assuming thus the same values of their recoilless Lamb-Mössbauer factors. An α -Fe foil
36 was used as calibration sample while the values of isomer shift are quoted relative to that of
37 α -Fe at 300 K.
38
39
40
41
42
43
44
45
46
47
48
49
50
51

52 **Computational Method.** We performed DFT calculations by using the Vienna Ab-initio
53 Software Package (VASP) program³⁶ with Perdew-Burke-Emzerhof (PBE) exchange-
54 correlation functional.³⁷ We investigated four slab models of magnetite; (2 × 1) Fe₃O₄ (111),
55
56
57
58
59
60

1
2
3 (2 × 2) Fe₃O₄ (220), (2 × 3) Fe₃O₄ (311), (3 × 1) Fe₃O₄ (400), (4 × 1) Fe₃O₄ (422) and (8 × 1)
4
5 Fe₃O₄ (511) surface, where bottom 1/3 layer was kept as fixed at a lattice point whereas the
6
7 upper layers were allowed to be fully relaxed (Figure S1). To prevent the interaction between
8
9 imaginary slab models along z-direction due to the periodic boundary condition, a vacuum
10
11 slab of ~ 20 Å perpendicular to the magnetite surface was included in the simulation cell. An
12
13 energy cutoff of 400 eV was used for the plane wave basis set and only the Gamma point was
14
15 sampled in the reciprocal space.
16
17
18
19
20
21

22 Results and Discussion

23
24
25 **Characterization of magnetite.** Morphological information for each magnetite (M1, M2, M3,
26
27 and M4) and their mineral identity were analyzed by TEM-selected area electron diffraction
28
29 (SAED) and SEM. Figure 1a and S2a show a spherical shape of M1 in the range of 10-20 nm.
30
31 The SAED pattern for M1 (Figure 1b) shows discontinuous circles which diameters
32
33 correspond to crystallographic planes of magnetite, i.e., 111, 220, and 311. The XRD pattern
34
35 of M1 (Figure S3) is indexed within the magnetite structure (space group $Fd\bar{3}m$, $a = 8.3640(6)$
36
37 Å). The average crystallite size analyzed by XRD was 13 nm (Table S1), which are in good
38
39 agreement with TEM results. Ideal magnetite has a $x = 0.5$ ratio of Fe²⁺/Fe³⁺ stoichiometry
40
41 but it becomes easily oxidized to nonstoichiometric magnetite ($x < 0.5$) by exposure to O₂ and
42
43 other oxidants in surrounding environment. The Fe²⁺/Fe³⁺ ratio for M1 using complete acid
44
45 dissolution was 0.19 (Table S2), being close to the Fe²⁺/Fe³⁺ ratio ($x = 0.2$) estimated by the
46
47 unit-cell length ($a = 8.3640(6)$) using a linear interpolation between Fe²⁺/Fe³⁺ stoichiometry
48
49 and reference unit-cell lengths.³⁸ Due to its very small particle size, the non-stoichiometry
50
51 character (or the partial oxidation) of M1 was expected, but accurate identification of
52
53 magnetite and maghemite in M1 cannot properly performed based only on XRD.³⁹ Mössbauer
54
55 spectroscopy can however provide relevant information on both the valency and spin states of
56
57
58
59
60

1
2
3 Fe species together with magnetic properties from the analysis of the hyperfine parameters.
4
5 The magnetic sextet with broadened and asymmetrical and a central quadrupolar component
6
7 observed in 300K Mössbauer spectrum of M1 (Figure S4) are characteristics of Fe³⁺ species,
8
9 attributed to ultrafine maghemite nanoparticles and larger single domain ones with slow
10
11 superparamagnetic relaxation phenomena. The latter behavior can be expected based on the
12
13 particle size previously estimated from X-ray patterns, and suggests a significant oxidation of
14
15 M1 nanoscale particles.
16
17

18
19 M2 shows a cubic morphology with particle sizes of 50–400 nm (Figures 1c and S2b)
20
21 and its SAED pattern (Figure 1d) is assigned to magnetite. The Fe²⁺/Fe³⁺ ratios for M2 were x
22
23 = 0.47 (HCl dissolution) and 0.54 (XRD), suggesting that M2 is the closest sample to the
24
25 magnetite stoichiometry in the present study. Higher than $x = 0.5$ ratio for M2 (XRD) may be
26
27 caused by the uncertainty of the linear interpolation in XRD analysis and HCl dissolution
28
29 method ($R^2 = 0.92$),³⁸ but still valuable to estimate the Fe²⁺/Fe³⁺ ratio. The average crystallite
30
31 size for M2 was 46 nm from XRD data. The larger particle and crystallite sizes for M2
32
33 compared to M1 could explain the higher resistance to oxidation and thus the higher x value.
34
35

36
37 M3 shows the mixture of non-uniform and cubic particles in the range of 100–500 nm
38
39 (Figures 1e and S2c). We observed that M3 contains some oxidized mineral form recognized
40
41 by the reflection 110 (i.e., maghemite) and a spot indicated by g (i.e., goethite, α -FeOOH) in
42
43 its SAED pattern (Figure 1f). This implies that traces of the completely oxidized form not
44
45 detected by XRD could be present in M3 due to the detection limit of the XRD analysis (1-
46
47 2 %). The Fe²⁺/Fe³⁺ ratios for M3 were $x = 0.42$ (HCl dissolution) and 0.48 (XRD) and the
48
49 average crystallite size for M3 was 45 nm.
50
51

52
53 M4 has distinct characteristics from other three magnetite. TEM and SEM images for
54
55 M4 show heterogeneous particle sizes (100 nm–10 μ m) with non-uniform shapes (Figures 1g
56
57 and S2d). The Fe²⁺/Fe³⁺ ratios for M4 were $x = 0.44$ (HCl dissolution) and 0.48 (XRD).
58
59 Interestingly, the average crystallite size was 54 nm, which is much smaller than particle sizes
60

1
2
3 observed by TEM and SEM. This indicates that M4 particles are polycrystalline. AFM
4 topographic images clearly shows that lateral fluctuations of surface features can be detected
5 in almost every 100 nm distance with 1–6 nm of topography deviation (Figure S5),
6
7 confirming that M4 particles are made of polycrystalline structured magnetite without
8 preferred orientated single crystals. Nevertheless, the relatively large particle and crystallite
9 sizes enable to isolate single crystalline domains and SAED pattern analysis clearly shows
10 individual spots corresponding to the $\bar{1}12$ zone axis of magnetite (Figure 1h).
11
12
13
14
15
16
17

18
19 As in case of magnetite, the Mössbauer spectra of M2, M3, and M4 can be described by
20 means of two components attributed to Fe^{3+} and $\text{Fe}^{2.5+}$ species, whereas the mean value of the
21 isomer shift is smaller suggesting some partial oxidation of magnetite. The hyperfine
22 structures can be decomposed into two ideal components corresponding to magnetite and
23 maghemite components (red and blue, respectively) (Figure S4). The estimates resulting from
24 their relative absorption area were 93:7, 70:30, and 83:17 for M2, M3, and M4 respectively,
25 which are rather in good agreement with the order of the $\text{Fe}^{2+}/\text{Fe}^{3+}$ ratio ($\text{M2} > \text{M4} > \text{M3}$)
26 (Table S2). Finally, the results obtained from BET shows the typical trend, i.e. decrease in
27 surface area from 75 to 1.7 m^2g^{-1} with respect to the increase in particle size from M1 to M4
28 (Table S2).
29
30
31
32
33
34
35
36
37
38
39
40
41
42

43 **Reduction of *p*-NP to *p*-AP by magnetite- NaBH_4 system.** The catalytic properties of each
44 magnetite sample were investigated using the reduction of *p*-NP to *p*-AP by NaBH_4 as a
45 model reaction (Figure S6). No significant reduction of *p*-NP was observed by NaBH_4
46 solution (100 mM), indicating that NaBH_4 alone cannot reduce *p*-NP under our experimental
47 conditions. In addition, all magnetite did not show any reduction of *p*-NP to *p*-AP without
48 addition of NaBH_4 , indicating that each magnetite does not directly reduce *p*-NP without
49 NaBH_4 in this study. The initial absorption peak of *p*-NP (317 nm) under acid and neutral
50 conditions was shifted to 400 nm after addition of NaBH_4 due to the formation of *p*-
51
52
53
54
55
56
57
58
59
60

1
2
3 nitrophenolate ions under basic condition ($\text{pH} > 11$).⁸ We did not observe any significant
4
5 change in the UV-vis spectra of M1, M2, and M3 suspensions after 120 min. TEM and SEM
6
7 images after the reaction of M1 revealed morphological changes in magnetite structure,
8
9 resulting in the non-uniformed shape of bigger particles than that of original M1 (Figure S7a-
10
11 d), while other M2 and M3 did not show any morphological change after the reaction (Figure
12
13 S7e-l). However, the morphological change of M1 does not seem to influence the catalytic
14
15 activity of M1 toward *p*-NP.
16

17
18 In contrast, M4 showed a remarkable decrease of the peak intensity at 400 nm together
19
20 with an increase of a new peak at 300 nm (Figure S6), which can be attributed to *p*-AP.^{23,40}
21
22 Based on the decrease in peak intensity at 400 nm (Figure S8), we can estimate that almost 70%
23
24 of initial *p*-NP was reduced after 120 minutes. This estimation was confirmed by HPLC
25
26 measurement after the reaction showing almost 62% of *p*-NP conversion with 70% of *p*-AP
27
28 production. This indicates that only M4 has an excellent catalytic activity toward the *p*-NP
29
30 reduction by NaBH_4 . The catalytic activity that is closely related to the NaBH_4 concentration
31
32 showed acceleration of *p*-NP reduction as the NaBH_4 concentration increased from 0 to 200
33
34 mM (Figure 2a). In particular, an induction time until 20 min was observed before initiating
35
36 the *p*-NP reduction and a linear decrease of the absorbance at 400 nm with increasing time
37
38 (Figure 2a), indicating pseudo-zero-order reduction kinetics. Furthermore, the zero-order
39
40 reduction kinetics seems proportional to the increase in NaBH_4 concentration (Figure 2b).
41
42 This result differs from that normally observed on various noble metallic catalysts showing
43
44 pseudo-first-order reduction kinetics without the presence of induction time.^{5,24,26} The
45
46 induction time has been observed in the presence of carbon materials (e.g., graphene and
47
48 natural polymer dextran) for the initial period for *p*-NP adsorption on the active sites of
49
50 carbon materials^{40,41} or in nanomaterials for a surface restructuring before the catalytic
51
52 reaction starts.⁴² Because more than 95% of conversion of *p*-AP from *p*-NP was achieved by
53
54 HPLC analysis, adsorption of *p*-NP on M4 can be considered as negligible. Furthermore, the
55
56
57
58
59
60

1
2
3 surface restructuring reaction is very fast, usually takes within 20 s not until 20 min,⁴² ruling
4
5 out such a phenomenon in our case. Moreover, no correlation between the catalytic activity of
6
7 magnetite and physicochemical properties such as particle size, BET or Fe²⁺/Fe³⁺ ratio was
8
9 observed. Therefore, other factors must undoubtedly control the catalytic reduction of *p*-NP
10
11 on the surface of M4.
12
13

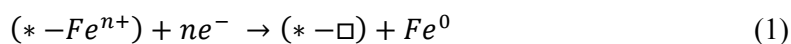
16 **Catalysis mechanism in magnetite-NaBH₄ suspension.** Electron microscopy and AFM
17
18 analysis were conducted to investigate the catalysis mechanism during the reaction of M4
19
20 with NaBH₄. Interestingly, we observed the formation of new aggregates of nanoparticles and
21
22 their attachment on M4 surface after reaction with NaBH₄ (Figure 3a). The magnified TEM
23
24 images (Figure 3c and d) clearly illustrated the spherical shape of the nanoparticles with < 50
25
26 nm diameter, which have amorphous SAED patterns with no clear lattice fringes and diffuse
27
28 rings likely elemental Fe nanoparticles (Figure 3b).⁴³ This is apparently different from the
29
30 typical SAED patterns of unreacted magnetite (Figure 3e). EDX mapping confirmed that new
31
32 nanoparticles mostly consist of Fe and O, without Na and B (Figure 3f), indicating that M4
33
34 formed Fe-based nanoparticles after the reaction with NaBH₄. SEM imaging also showed a
35
36 cauliflower structure on the surface of M4 (Figure S9a). Consequently, the formation of
37
38 elemental Fe nanoparticles on M4 surfaces after reaction with NaBH₄ may explain the great
39
40 catalytic activity of M4, as we have recently observed for synthetic zero valent iron in the
41
42 presence of NaBH₄.²⁹
43
44
45
46

47 In addition, the formation of cracks on the M4 surface was observed after the reaction
48
49 (Figure S9b). AFM surface images of microscale M4 before (Figure 4a) and after (Figure 4b)
50
51 the addition of NaBH₄ strongly supports the dramatic surface changes observed at different
52
53 scales by both SEM and TEM. A relatively smooth surface of pristine M4 (Figure 4c) was
54
55 significantly changed to be highly rough in a macroscale point of view (Figure 4d). The direct
56
57 comparison of topography deviation with and without NaBH₄ clearly shows the evolution of
58
59
60

1
2
3 spikes (i.e., Fe nanoparticles) with the formation of deep macroscopic crack (approximately
4 125 nm with reference to the non-reacted surface plane) on the surface of M4. To investigate
5 the more precise formation mechanism of elemental Fe nanoparticles, high resolution (HR)
6 TEM was conducted using 6 h reaction sample with NaBH₄ without *p*-NP (Figure 5). The
7 formation of cracks on outer surfaces of M4 (Figure 5a) and nanoparticles possessing inner
8 crystal lattices are observed. The SAED pattern of the inner crystal lattices revealed the
9 magnetite peaks 311m, 400m, and 422m, but we do not see the 222m and 111m peaks present
10 on other crystallites. We thus suggest the presence of wüstite (FeO) which 111w and 200w
11 peaks are superimposed with 311m and 400m, respectively, as these two peaks are most
12 intense for this phase. This implies that wüstite could be intermediate phase in the reductive
13 reaction of M4 to elemental Fe nanoparticles.
14
15
16
17
18
19
20
21
22
23
24
25
26

27 Although the formation mechanism of typical elemental Fe nanoparticles synthesized by
28 Fe³⁺-NaBH₄ solution system is unclear to date, it might involve the classic crystal formation
29 caused by spontaneous formation of nuclei and their growth up to a critical size as normally
30 observed in crystal formation from solution.⁴⁴ Interestingly, the formation mechanism of
31 elemental metallic Fe nanoparticles from M4-NaBH₄ system seems to be as pre-nucleation
32 cluster induced crystal formation.⁴⁵ Hua and Huang have reported that microscale magnetite
33 octahedra can be transformed to magnetite single crystal microplates by NaBH₄ called in
34 “chemical etching process”.⁴⁶ Here, we observe the formation of tiny nanoparticles and their
35 aggregation giving rise to larger particles as evidenced by TEM and AFM (Figure S10a and c).
36 Particle size analysis from AFM also reveals that the dominant size of particles without
37 NaBH₄ varied from 100–260 nm (64%) to larger size < 2 μm, while the sample with NaBH₄
38 showed 63% of tiny nanoparticles (< 45 nm) with other small sized nanoparticles (< 280 nm)
39 (Figure S10d). Furthermore, a monodisperse size distribution of tiny bead shaped
40 nanoparticles (less than 2 nm) was observed at outer layers (Figure 5b and c), indicating that
41 elemental Fe nanoparticles may form through the aggregation of nanometric building blocks.
42
43
44
45
46
47
48
49
50
51
52
53
54
55
56
57
58
59
60

DFT calculation. It has been hypothesized that surface defects of magnetite (e.g., edge and corner sites, shallow walls of phase boundaries, and bridge between each single crystal), possibly less thermodynamically stable relative to the highly coordinated surface, may provide the specific reactive sites for NaBH_4 ,³⁰ and thus explain the greater reactivity of magnetite. However, it is still unclear which surface index on magnetite is predominantly reacted with NaBH_4 . To investigate the surface index dependent activity of magnetite, we used DFT calculations in this study. The net reaction of *p*-NP reduction with NaBH_4 in an alkaline aqueous solution is $p\text{-NP} + 3\text{NaBH}_4 + \text{H}_2\text{O} \rightarrow p\text{-AP} + 3\text{NaOH} + 3\text{BH}_3$.³⁰ Based on the well-known Bell-Evans-Polyanyi principle,^{47,48} the binding energy of BH_3 to the magnetite surface ($\Delta E_{\text{b}}^{\text{BH}_3}$) can be conceived as a good activity descriptor when the magnetite surface is involved in the reaction as a catalyst. Figure 6 shows DFT calculated $\Delta E_{\text{b}}^{\text{BH}_3}$ values for the most stable configuration of BH_3 on the six different surface slab models of magnetite: (111), (220), (311), (400), (422), and (511). We found that the binding affinity becomes substantial generally for the high index surfaces, leading to a close interaction between BH_3 and surface-exposed Fe. Particularly, Fe metals exposed on the (400) and (511) surfaces show the strongest interaction with BH_3 . We further calculated the electrochemical potential for leaching Fe out from the magnetite surface and forming an elemental Fe ($\varepsilon_{\text{Fe}}^0$). The electrochemical reaction is written as following:



where n means the number of electrons that is 3, and the asterisk denotes the magnetite surface bound state. We calculated the reaction energy (ΔE) associated with above reaction (Eq. 1), which is approximated to the reaction free energy, $\Delta G \approx \Delta E$. We then calculated $\varepsilon_{\text{Fe}}^0$

1
2
3 using Nernst equation; $\Delta G = -nF\varepsilon_{Fe}^0$, and ε_{Fe}^0 is referenced to 4.44 V to denote it versus
4
5 standard hydrogen electrode (SHE).⁴⁹ The results suggest that ε_{Fe}^0 shows the same tendency
6
7 to the change of $\Delta E_b^{BH_3}$ for various surfaces; higher reduction potential for high index
8
9 surfaces. We further observed that ε_{Fe}^0 of (400) and (511) surfaces increased up to ~ 1 V
10
11 compared to the most stable (111) surface. This indicates that Fe exposed at the high index
12
13 magnetite surface can be much easily leached out to form an elemental Fe that can further be
14
15 utilized for the *p*-NP reduction. We, therefore, anticipate that M4 may possess much high
16
17 index surface at its surface defects, leading to the intensive interaction between the surface
18
19 and NaBH₄.
20
21
22
23
24
25

26 **Catalytic activity and stability of polycrystalline magnetite.** To assess the catalytic
27
28 stability of polycrystalline magnetite in NaBH₄ system, *p*-NP reduction (or *p*-AP production)
29
30 was determined up to ten reaction cycles. The rationale of these experiments is two-fold: (i)
31
32 compare the catalytic recyclability of M4 with other metallic catalysts, which normally shows
33
34 deactivation as the number of reaction cycle increased^{5,8,28,50,51}; and (ii) get better insights
35
36 about the reaction kinetics and mechanisms.
37
38

39 Surprisingly, the reduction kinetics of *p*-NP was kept increasing significantly until 3rd
40
41 cycle and then reached a steady state (i.e. constant kinetic rate of 0.132 min⁻¹ within the error
42
43 value, Figure 7a and b). We also observed the almost complete conversion of *p*-NP to *p*-AP
44
45 by HPLC analysis after each reaction of 30 min (Figure 7c). It should be noted that the
46
47 reduction kinetics seems to be changed from zero-order kinetics to first-order kinetics from 3rd
48
49 cycle ($R^2 > 0.95$). This suggests that both formation of elemental Fe nanoparticles and
50
51 subsequent catalytic reaction simultaneously proceeded during the 1st and 2nd cycles. The
52
53 reduction kinetics of *p*-NP might be governed by the formation kinetics of elemental Fe
54
55 nanoparticles, resulting in the zero-order-kinetics. After 3rd cycle, the formation of elemental
56
57
58
59
60

1
2
3 Fe nanoparticles may be terminated due to the limited surface of M4. Then the generated
4 nanoparticles previously can continue the catalytic reduction of *p*-NP with a typical first-
5 order-kinetic without deactivation process up to 10 times recycle. To confirm both the
6 enhanced catalytic activity during 1st to 3rd cycles and the constant catalytic activity after 3rd
7 cycle, the production of H₂ was measured after 1st, 3rd, 5th, and 10th cycles (Table S3). It is
8 known that the production reaction of H₂ from NaBH₄ solution is exothermic (NaBH₄
9 (-188.61 kJ) + 2H₂O (-571.66 kJ) → NaBO₂ (-977.0 kJ) + 4H₂ (0 kJ) at 25 °C) and its
10 reaction can be accelerated by catalysts.⁵² The percentage of H₂ after 1st cycle (120 min) was
11 29.8%, which is almost similar to the control 1 (120 min reaction without M4), while its value
12 significantly increased at 3rd cycle (42.6%) in 30 min. This amount was 3.5 times higher than
13 that of control 2 (30 min reaction without M4), underscoring the enhanced catalytic activity of
14 M4 with NaBH₄ solution. The H₂ production at 5th (43.2%) and 10th (45.4%) cycles was very
15 similar to the 3rd cycle within the error values, confirming the constant catalytic activity of
16 M4 after 3rd cycle.
17
18
19
20
21
22
23
24
25
26
27
28
29
30
31
32

33
34 The 300K Mössbauer spectra of M4 submitted to several reaction cycles clearly showed
35 changes growing at the central part of the spectra with the emergence of quadrupolar
36 component which turns into a strongly broadened line (Figure 8). The proportion of this
37 quadrupolar component (green line) is estimated at about 2 % in M4 1 time, whereas the
38 isomer shift value (0.95 mm/s) suggests Fe²⁺ which could be attributed to non-stoichiometric
39 FeO phase. The central quadrupolar component becomes more important in M4 5th times
40 (estimated at about 10-12 %) but the isomer shift value is rather consistent with the presence
41 of elemental metallic Fe. For the 10th times sample, this component significantly increased up
42 to about 30-35% (Figure 8). The 77K Mössbauer spectrum of the latter sample showed first
43 an external magnetic component which exhibits a complex hyperfine structure resulting
44 typically from the superimposition of maghemite contribution and that of magnetite as below
45
46
47
48
49
50
51
52
53
54
55
56
57
58
59
60

1
2
3 the Verwey transition. In addition, a magnetic feature (estimated at about 30%) occurred at
4
5 the center which can be assigned to metallic Fe species.
6
7

8 9 **Conclusions**

10
11 On the basis of all these findings, we can propose the reaction mechanism scheme depicted in
12
13 Figure 9: i.e. the reaction of NaBH₄ with most high index surfaces at its surface defects of
14
15 polycrystalline magnetite can result in pre-nucleation cluster induced crystal formation of
16
17 critical size of tiny Fe⁰ nanoparticles (~ 2 nm) via its intermediate phase (i.e., FeO). The
18
19 newly formed elemental Fe nanoparticles are then attracted on top of mother magnetite by
20
21 their instinctive magnetism and/or get assembled to grow to larger particle size. The various
22
23 surface and catalytic investigations revealed that elemental Fe nanoparticles formed on the
24
25 surface of polycrystalline magnetite after the reaction with NaBH₄ are probably responsible
26
27 for the sustainable catalytic activity. However, these newly generated elemental Fe
28
29 nanoparticles cannot reduce *p*-NP without further NaBH₄ addition. Indeed, the *p*-NP reduction
30
31 only occurs when NaBH₄ was added into the suspension during 10 times recycles in
32
33 sequencing injection of NaBH₄ and DIW, whereas kinetic rate constant increased as the
34
35 reaction cycle increased (i.e., up to ~ 0.131 min⁻¹) (Figure S11). Furthermore, the catalytic
36
37 activity of polycrystalline magnetite is preserved, which could overcome the deactivation
38
39 problem generally encountered in other metallic nanoscale catalysts. As the catalytic
40
41 reduction methods including dechlorination and hydrogenation of nitroaromatic compounds
42
43 are often carried out under an atmosphere of H₂ (hydrogen source), the experimental and
44
45 theoretical results from this study can highlight the important dual role of NaBH₄: (i) acting as
46
47 a hydrogen donor, and (ii) producing highly reactive nanoparticles on the surface of catalyst.
48
49
50
51
52

53
54 Although polycrystalline magnetite possesses much larger particle size (or lower surface
55
56 area), it shows a remarkable catalytic activity compared to single crystalline magnetite. This
57
58 counter-intuitive finding (because the greater reactivity of nanoscale materials is generally
59
60

1
2
3 admitted) calls for more attention to the assessment of intrinsic reactivity of used materials in
4 heterogeneous catalysis. As there is a growing interest in environmentally friendly catalytic
5 processes based on magnetic solids, the remarkable catalytic recyclability of polycrystalline
6 magnetite offers a strong potential for developing cheap and effective magnetic catalysts
7 without use of noble precious metals. Furthermore, because synthesis methods for
8 polycrystalline magnetite are becoming increasingly developed,⁵³ we thus anticipate our
9 findings to be a starting point for investigating other unknown properties of polycrystalline
10 magnetite in other-disciplinary researches such as semiconductor, biomedicine, and
11 environmental remediation.
12
13
14
15
16
17
18
19
20
21
22
23
24

25 **Supporting Information**

26
27 The Supporting Information is available free of charge on the ACS Publications website at
28 DOI:
29

30
31 Details of the material characterization (i.e., XRD, SEM, Mössbauer, AFM, and TEM)
32 and additional results for reduction of p-NP by four different magnetite.
33
34
35
36
37
38
39

40 **Acknowledgments**

41
42 We would like to thank the “Région Bretagne” for financial support (Contract SAED-
43 ReSolEau (8256)) for the most of experiments and THEMIS for TEM experiments. We also
44 acknowledge the support by the National Research Foundation of Korea (project no.
45 2016R1D1A1B03930142).
46
47
48
49
50
51
52
53
54

55 **References**

- 1
2
3 (1) Zaera, F. Nanostructured materials for applications in heterogeneous catalysis. *Chem. Soc.*
4
5 *Rev.* **2013**, *42*, 2746–2762.
- 6
7 (2) Gawand, M. B.; Branco, P. S.; Varma, R. Nano-magnetite (Fe₃O₄) as a support for
8
9 recyclable catalysts in the development of sustainable methodologies. *Chem. Soc. Rev.*
10
11 **2013**, *42*, 3371–3393.
- 12
13 (3) Wunder, S.; Polzer, F.; Lu, Y.; Mei, Y.; Ballauff, M. Kinetic analysis of catalytic
14
15 reduction of 4-nitrophenol by metallic nanoparticles immobilized in spherical
16
17 polyelectrolyte brushes. *J. Phys. Chem. C* **2010**, *114*, 8814–8820.
- 18
19 (4) Jana, S.; Ghosh, S. K.; Nath, S.; Pande, S.; Praharaj, S.; Panigrahi, S.; Basu, S.; Endo, T.;
20
21 Pal, T. Synthesis of silver nanoshell-coated cationic polystyrene beads: A solid phase
22
23 catalyst for the reduction of 4-nitrophenol. *Appl. Catal., A: Gen.* **2006**, *313*, 41–48.
- 24
25 (5) Lin, F-H.; Doong, R-A. Highly efficient reduction of 4-nitrophenol by heterostructured
26
27 gold-magnetite nanocatalysts. *Appl. Catal., A: Gen.* **2014**, *486*, 32–41.
- 28
29 (6) Shin, K. S.; Cho, Y. K.; Choi, J-Y.; Kim, K. Facile synthesis of silver-deposited silanized
30
31 magnetite nanoparticles and their application for catalytic reduction of nitrophenols. *Appl.*
32
33 *Catal., A:* **2012**, *413–414*, 170–175.
- 34
35 (7) Li, J.; Liu, C.-y; Liu, Y. Au/graphene hydrogel: Synthesis, characterization and its use for
36
37 catalytic reduction of 4-nitrophenol. *J. Mater. Chem.* **2012**, *22*, 8426–8430.
- 38
39 (8) Lin, F-H.; Doong, R-A. Bifunctional Au-Fe₃O₄ heterostructures for magnetically
40
41 recyclable catalysis of nitrophenol reduction. *J. Phys. Chem. C* **2011**, *115*, 6591–6598.
- 42
43 (9) Shin, H.; Jung, S.; Bae, S.; Kim, H.; Lee, W. Nitrate reduction mechanism on a Pd
44
45 surface. *Environ. Sci. Technol.* **2014**, *48*, 12768–12774.
- 46
47 (10) Jung, S.; Bae, S.; Lee, W. Development of Pd-Cu/hematite catalyst for selective nitrate
48
49 reduction. *Environ. Sci. Technol.* **2014**, *48*, 9651–9658.
- 50
51 (11) Jung, J.; Bae, S.; Lee, W. Nitrate reduction by maghemite supported Cu-Pd bimetallic
52
53 catalyst. *Appl. Catal. B- Environ.* **2012**, *127*, 148–158.
- 54
55
56
57
58
59
60

- 1
2
3 (12) Xu, Z. C.; Shen, C. M.; Hou, Y. L.; Gao, H. J.; Sun, S. S. Oleylamine as both reducing
4 agent and stabilizer in a facile synthesis of magnetite nanoparticles. *Chem. Mater.* **2009**,
5 *21*, 1778–1780.
6
7
8
9 (13) Rostamizadeh, S.; Shadjou, N.; Azad, M.; Jalali, N. (α -Fe₂O₃)-MCM-41 as a
10 magnetically recoverable nanocatalyst for the synthesis of pyrazolo[4,3-c]pyridines at
11 room temperature. *Catal. Commun.* **2012**, *26*, 218–224.
12
13
14 (14) Ramimoghadam, D.; Bagheri, S.; Hamid, S. B. A. Progress in electrochemical synthesis
15 of magnetic iron oxide nanoparticles. *J. Magn. Magn. Mater.* **2014**, *368*, 207–229.
16
17
18 (15) Yang, C.; Wu, J.; Hou, Y. Fe₃O₄ nanostructures: synthesis, growth mechanism,
19 properties and applications. *Chem. Commun.* **2011**, *47*, 5130–5141.
20
21
22 (16) Qi, H. P.; Chen, Q. W.; Wang, M. S.; Wen, M. H.; Xiong, J. Study of self-assembly of
23 octahedral magnetite under an external magnetic field. *J. Phys. Chem. C* **2009**, *113*,
24 17301–17305.
25
26
27 (17) Zhang, L. H.; Wu, J. J.; Liao, H. B.; Hou, Y. L.; Gao, S. Octahedral Fe₃O₄ nanoparticles
28 and their assembled structures. *Chem. Commun.* **2009**, *29*, 4378–4380.
29
30
31 (18) Liu, F.; Cao, P. J.; Zhang, H. R.; Tian, J. F.; Xiao, C. W.; Shen, C. M.; Li, J. Q.; Gao, H. J.
32 Novel nanopyramid arrays of magnetite. *Adv. Mater.* **2005**, *17*, 1893–1897.
33
34
35 (19) Gorski, C. A.; Nurmi, J. T.; Tratnyek, P. G.; Hofstetter, T. B.; Scherer, M. M. Redox
36 behavior of magnetite: Implications for contaminant reduction. *Environ. Sci.*
37 *Technol.* **2010**, *44*, 55–60.
38
39
40 (20) Cornell, R. M.; Schwertmann, U. *The Iron Oxides: Structure, Properties, Reactions,*
41 *Occurrences and Uses*, 2nd ed., pp. 185–407, Wiley-VCH Verlag GmbH & Co.
42 KGaA, Weinheim, FRG, Germany, 2003.
43
44
45 (21) Daniels, J. M.; Rosencwaig, A. Mössbauer spectroscopy of stoichiometric and non-
46 stoichiometric magnetite. *J. Phys. Chem. Solids* **1969**, *30*, 1561–1571.
47
48
49
50
51
52
53
54
55
56
57
58
59
60

- 1
2
3 (22) Hervés, P.; Perez-Lorenzo, M.; Liz-Marzan, L. M.; Dzubielia, J.; Lu, Y.; Ballauff, M.
4
5 Catalysis by metallic nanoparticles in aqueous solution: Model reactions. *Chem. Soc.*
6
7 *Rev.* **2012**, *41*, 5577–5587.
8
9
10 (23) An, M.; Cui, J.; Wang, L. Magnetic recyclable nanocomposite catalysts with good
11
12 dispersibility and high catalytic activity. *J. Phys. Chem. C* **2014**, *118*, 3062–3068.
13
14 (24) Zhang, P.; Li, R.; Huang, Y.; Chen, Q. A. Novel approach for the in situ synthesis of Pt–
15
16 Pd nanoalloys supported on Fe₃O₄@C core–shell nanoparticles with enhanced catalytic
17
18 activity for reduction reactions. *ACS Appl. Mater. Interfaces* **2014**, *6*, 2671–2678.
19
20 (25) Song, J. M.; Zhang, S. S.; Yu, S. H. Multifunctional Co_{0.85}Se-Fe₃O₄ nanocomposites:
21
22 controlled synthesis and their enhanced performances for efficient hydrogenation of *p*-
23
24 nitrophenol and adsorbents. *Small* **2014**, *10*, 717–724.
25
26
27 (26) Wang, Q.; Jia, W.; Liu, B.; Dong, A.; Gong, X.; Li, C.; Jing, P.; Li, Y.; Xu, G.; Zhang, J.
28
29 Hierarchical structure based on Pd(Au) nanoparticles grafted onto magnetite cores and
30
31 double layered shells: enhanced activity for catalytic applications. *J Mater Chem A* **2013**,
32
33 *1*, 12732–12741.
34
35
36 (27) Xu, R.; Bi, H.; He, G.; Zhu, J.; Chen, H. Synthesis of Cu-Fe₃O₄@graphene composite: a
37
38 magnetically separable and efficient catalyst for the reduction of 4-nitrophenol. *Mater.*
39
40 *Res. Bull.* **2014**, *57*, 190–196.
41
42
43 (28) Du, X.; He, J.; Zhu, J.; Sun, L.; An, S. Ag-deposited silica-coated Fe₃O₄ magnetic
44
45 nanoparticles catalyzed reduction of *p*-nitrophenol. *Appl. Surf. Sci.* **2012**, *258*, 2717–2723.
46
47
48 (29) Bae, S. & Hanna, K. Reactivity of nanoscale zero valent iron in unbuffered systems:
49
50 Effect of pH and Fe(II) dissolution. *Environ. Sci. Technol.* **2015**, *49*, 10536–10543.
51
52
53 (30) Bae, S.; Gim, S.; Kim, H.; Hanna, K. Effect of NaBH₄ on properties of nanoscale zero-
54
55 valent iron and its catalytic activity for reduction of *p*-nitrophenol. *Appl. Catal. B-*
56
57 *Environ.* **2016**, *127*, 148–158.
58
59
60

- 1
2
3 (31) Usman, M.; Abdelmoula, M.; Hanna, K.; Grégoire, B.; Faure, P.; Ruby, C. Fe^{II} induced
4 mineralogical transformations of ferric oxyhydroxides into magnetite of variable
5 stoichiometry and morphology. *J. Solid State Chem.* **2012**, *194*, 328–335.
6
7
8
9
10 (32) Stookey, L. L. Ferrozine-A new spectrophotometric reagent for iron. *Anal. Chem.* **1970**,
11 *42*, 779–781.
12
13
14 (33) Bae, S.; Lee, W. Influence of riboflavin on nanoscale zero-valent iron reactivity during
15 the degradation of carbon tetrachloride. *Environ. Sci. Technol.* **2014**, *48*, 2368–2376.
16
17
18 (34) Rodriguez-Carvajal, J. Recent advances in magnetic-structure determination by neutron
19 powder diffraction. *Physica B* **1993**, *192*, 55–69.
20
21
22 (35) Rodriguez-Carvajal, J.; Roisnel, T. Line broadening analysis using Fullprof:
23 Determination of microstructural properties. *Materials Science Forum* **2004**, *443–444*,
24 *123–126*.
25
26
27
28
29 (36) Kresse J. G.; Furthmuller. J. Efficient iterative schemes for ab initio total-energy
30 calculations using a plane-wave basis set. *Phys. Rev. B* **1996**, *54*, 11169–11186.
31
32
33 (37) Perdew, J. P.; Burke, K.; Ernzerhof, M. Generalized gradient approximation made simple.
34 *Phys. Rev. Lett.* **1996**, *77*, 3865–3868.
35
36
37
38 (38) Gorski, C. A.; Scherer, M. M. Determination of nanoparticulate magnetite stoichiometry
39 by Mössbauer spectroscopy, acidic dissolution, and powder X-ray diffraction: A critical
40 review. *Am. Mineral.* **2010**, *95*, 1017– 1026.
41
42
43
44 (39) Kim, W.; Suh, C.-Y.; Cho, S.-W.; Roh, K.-M.; Kwon, H.; Song, K.; Shon, I.-J. A new
45 method for the identification and quantification of magnetite–maghemite mixture using
46 conventional X-ray diffraction technique. *Talanta* **2012**, *94*, 348– 352.
47
48
49
50 (40) Kong, X. K.; Sun, Z. Y.; Chen, M.; Chen, Q. W. Metal-free catalytic reduction of 4-
51 nitrophenol to 4-aminophenol by N-doped graphene. *Energy Environ. Sci.* **2013**, *6*, 3260–
52 3266.
53
54
55
56
57
58
59
60

- 1
2
3 (41) Lara, L. R.; Zottis, A. D.; Elias, W. C.; Faggion, D.; de Campos, C. E. M.; Acuña, J. J. S.;
4
5 Domingos, J. B. The catalytic evaluation of *in situ* grown Pd nanoparticles on the surface
6
7 of Fe₃O₄@dextran particles in the *p*-nitrophenol reduction reaction. *RSC Adv.* **2015**, *5*,
8
9 8289–8296.
10
11 (42) Gu, S.; Wunder, S.; Lu, Y.; Ballauff, M. Kinetic analysis of the catalytic reduction of 4-
12
13 nitrophenol by metallic nanoparticles. *J. Phys. Chem. C* **2014**, *118*, 18618–18625.
14
15 (43) Wang, Q. L.; Kanel, S. R.; Park, H.; Ryu, A.; Choi, H. Controllable synthesis,
16
17 characterization, and magnetic properties of nanoscale zerovalent iron with specific high
18
19 Brunauer–Emmett–Teller surface area. *J. Nanopart. Res.* **2009**, *11*, 749–755.
20
21 (44) Kashchiev, D. *Nucleation: Basic Theory with Applications*, Butterworth-
22
23 Heinemann, Oxford, 2000.
24
25 (45) Banfield, J. F.; Welch, S. A.; Zhang, H.; Ebert, T. T.; Penn, R. L. Aggregation-based
26
27 crystal growth and microstructure development in natural iron oxyhydroxide
28
29 biom mineralization products. *Science* **2000**, *289*, 751–754.
30
31 (46) Hua, Q.; Huang, W. Chemical etching induced shape change of magnetite microcrystals.
32
33 *J. Mater. Chem.* **2008**, *18*, 4286–4290.
34
35 (47) Bell, R. P. The theory of reactions involving proton transfers. *Proc. R. Soc. London, Ser.*
36
37 *A* **1936**, *154*, 414–429.
38
39 (48) Evans, M. G.; Polanyi, M. Further considerations on the thermodynamics of chemical
40
41 equilibria and reaction rates. *Trans. Faraday Soc.* **1936**, *32*, 1333–1360.
42
43 (49) Trasatti, S. Interfacial behavior of non-aqueous solvents. *Electrochim. Acta* **1987**, *31*,
44
45 843–850.
46
47 (50) Zhang, P.; Sui, Y.; Xiao, G.; Wang, Y.; Wang, C.; Liu, B.; Zou, G.; Zou, B. Facile
48
49 fabrication of faceted copper nanocrystals with high catalytic activity for *p*-nitrophenol
50
51 reduction. *J. Mater. Chem. A* **2013**, *1*, 1632–1638.
52
53
54
55
56
57
58
59
60

- 1
2
3 (51) Wu, Y.-G.; Wen, M.; Wu, Q.-S.; Fang, H. Ni/graphene nanostructure and its electron-
4 enhanced catalytic action for hydrogenation reaction of nitrophenol. *J. Phys. Chem. C*
5 **2014**, *118*, 6307–6313.
6
7
8
9 (52) Kojima, Y.; Suzuki, K.; Fukumoto, K.; Sasaki, M.; Yamamoto, T.; Kawai, Y.; Hayashi,
10 H. Hydrogen generation using sodium borohydride solution and metal catalyst coated on
11 metal oxide. *Int. J. Hydrogen Energy* **2002**, *27*, 1029–1034.
12
13
14
15 (53) Mantovan, R.; Lamperti, A.; Georgieva, M.; Tallarida, G.; Fanciulli, M. CVD synthesis
16 of polycrystalline magnetite thin films: structural, magnetic and magnetotransport
17 properties. *J. Phys. D: Appl. Phys.* **2010**, *43*, 065002-1.
18
19
20
21
22
23
24
25
26
27
28
29
30
31
32
33
34
35
36
37
38
39
40
41
42
43
44
45
46
47
48
49
50
51
52
53
54
55
56
57
58
59
60

Figures

Figure 1. TEM images and SAED patterns of four different magnetite samples: (a and b) M 1, (c and d) M2, (e and f) M3, and (g and h) M4.

Figure 2. Reduction kinetics of *p*-NP by M4-NaBH₄ system: (a) Effect of NaBH₄ concentration on the reduction of *p*-NP showing the pseudo-zero-order reaction kinetics and (b) change in k_{obs} with respect to the NaBH₄ concentration.

Figure 3. TEM results for M4 after the reaction: (a) TEM images after the 1st reaction of M4 showing both (b) the amorphous SAED pattern of spherical shape of nanoparticles (c and d) and (e) the magnetite SAED pattern of original M4. (f) STEM Bright field image and EDX mapping showing the elemental distribution on the surface.

Figure 4. AFM results before and after the reaction: AFM images of M4 (a) before and (b) after the reaction and their 3D topographic images (c and d). (e) The different topography deviation of M4 (indicated by arrow in (a) and (b)) showing the evolution of spikes and formation of cracks after the reaction.

Figure 5. HR-TEM results for M4 after the reaction: TEM images show (a) the crack formation and (b) small nanoparticles gathering on top of M4 surface. (c and d) The inner structure of intermediate phase revealed both the magnetite and *wüstite* SAD patterns. (e) *Final structure of M4 after the reaction.*

Figure 6. Results of DFT calculation: the results showed BH₃ binding energies ($\Delta E_{\text{b}}^{\text{BH}_3}$), B-Fe binding distances, and electrochemical reduction potential for leaching Fe out from the

1
2
3 surface ($\varepsilon_{\text{Fe}}^0$ vs. SHE), which are calculated for various magnetite slab models of (2×1)
4
5 Fe_3O_4 (111), (2×2) Fe_3O_4 (220), (2×3) Fe_3O_4 (311), (3×1) Fe_3O_4 (400), (4×1) Fe_3O_4 (422)
6
7 and (8×1) Fe_3O_4 (511) surfaces. $n = 3$ as formal charge of exposed Fe atom was chosen
8
9 when $\varepsilon_{\text{Fe}}^0$ is calculated using Eq. (1).
10
11
12
13

14 **Figure 7.** Recycling test: (a) Reduction kinetics of *p*-NP by M4 with NaBH_4 during the 10
15 time recycling test, (b) pseudo-first-order kinetics from 2nd cycle and their mean k_{obs} value
16 (green line) with standard deviation (shaded area), and (c) the conversion efficiency after
17 finishing each cycle.
18
19
20
21
22
23
24

25 **Figure 8.** 300K Mössbauer spectra recorded on the as-prepared M4 and M4 submitted to
26 different cycling treatments and 77K Mössbauer spectrum on M4 submitted to 10 times
27 cycling treatments; red and blue curves correspond to ideal magnetite and maghemite
28 magnetic components at 300K, respectively, while the green curve is ascribed to the last
29 component as described in the text.
30
31
32
33
34
35
36
37
38

39 **Figure 9.** (a) Conceptual atomic diagram showing the enhanced disintegration of magnetite
40 by NaBH_4 as the index surface increases and (b) catalytic mechanism proposed by this study.
41
42 Red, purple, orange, cyan, white, grey circles and sticks denote oxygen, iron, boron, sodium,
43 hydrogen, carbon, respectively.
44
45
46
47
48
49
50
51
52
53
54
55
56
57
58
59
60

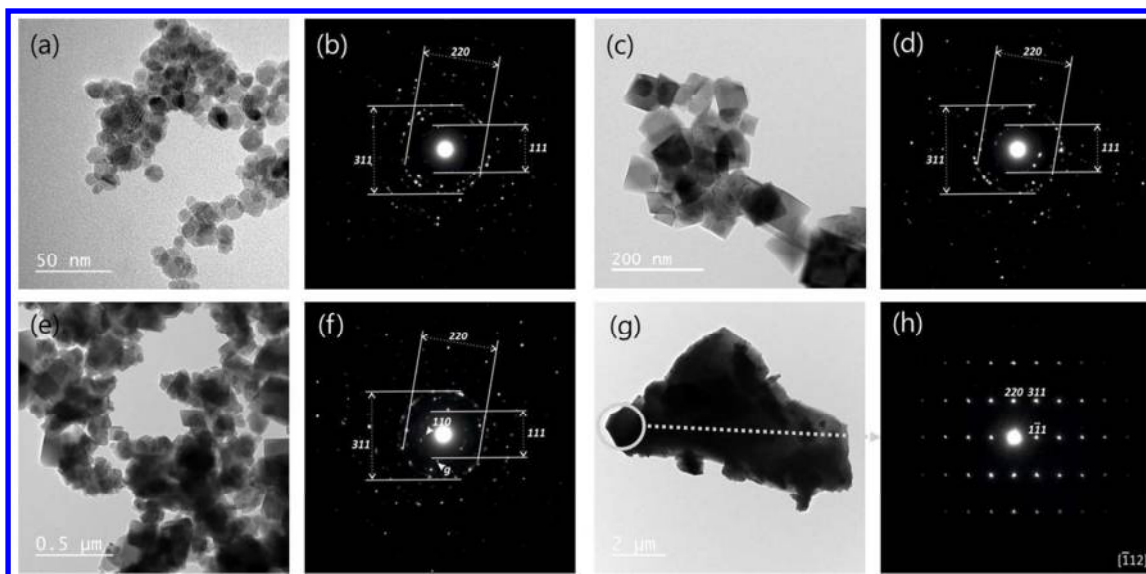


Figure 1

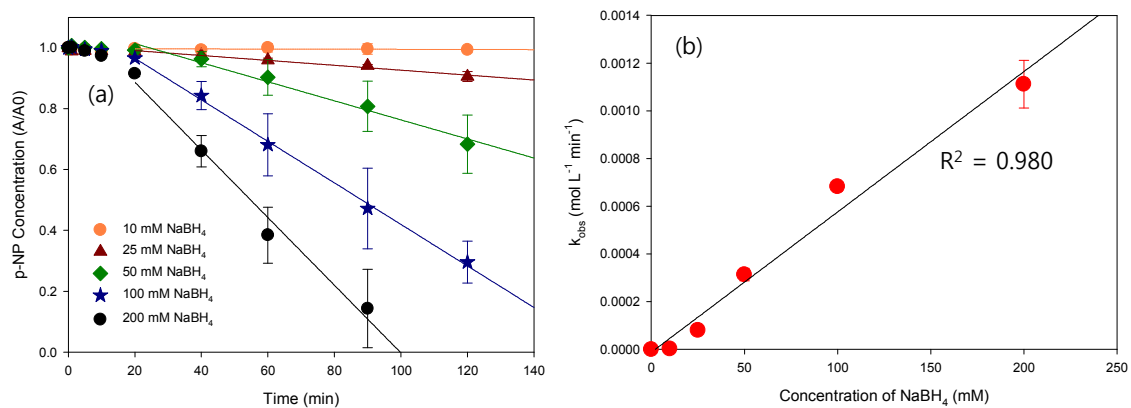


Figure 2

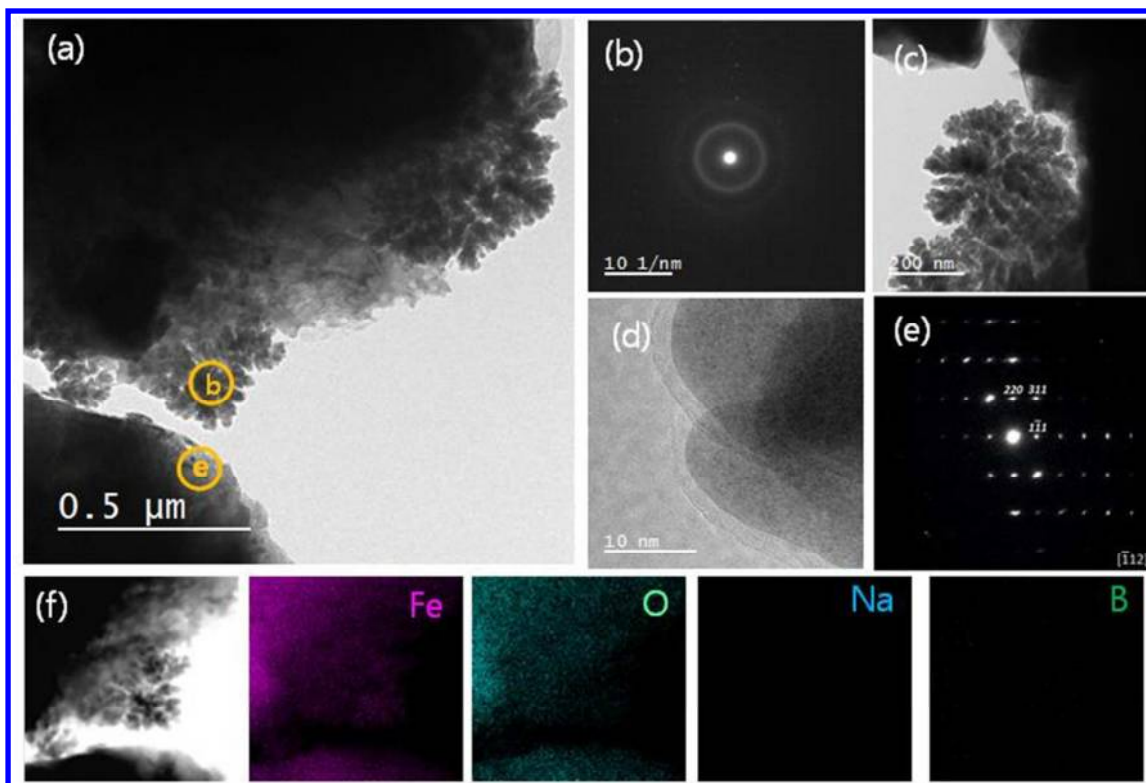


Figure 3

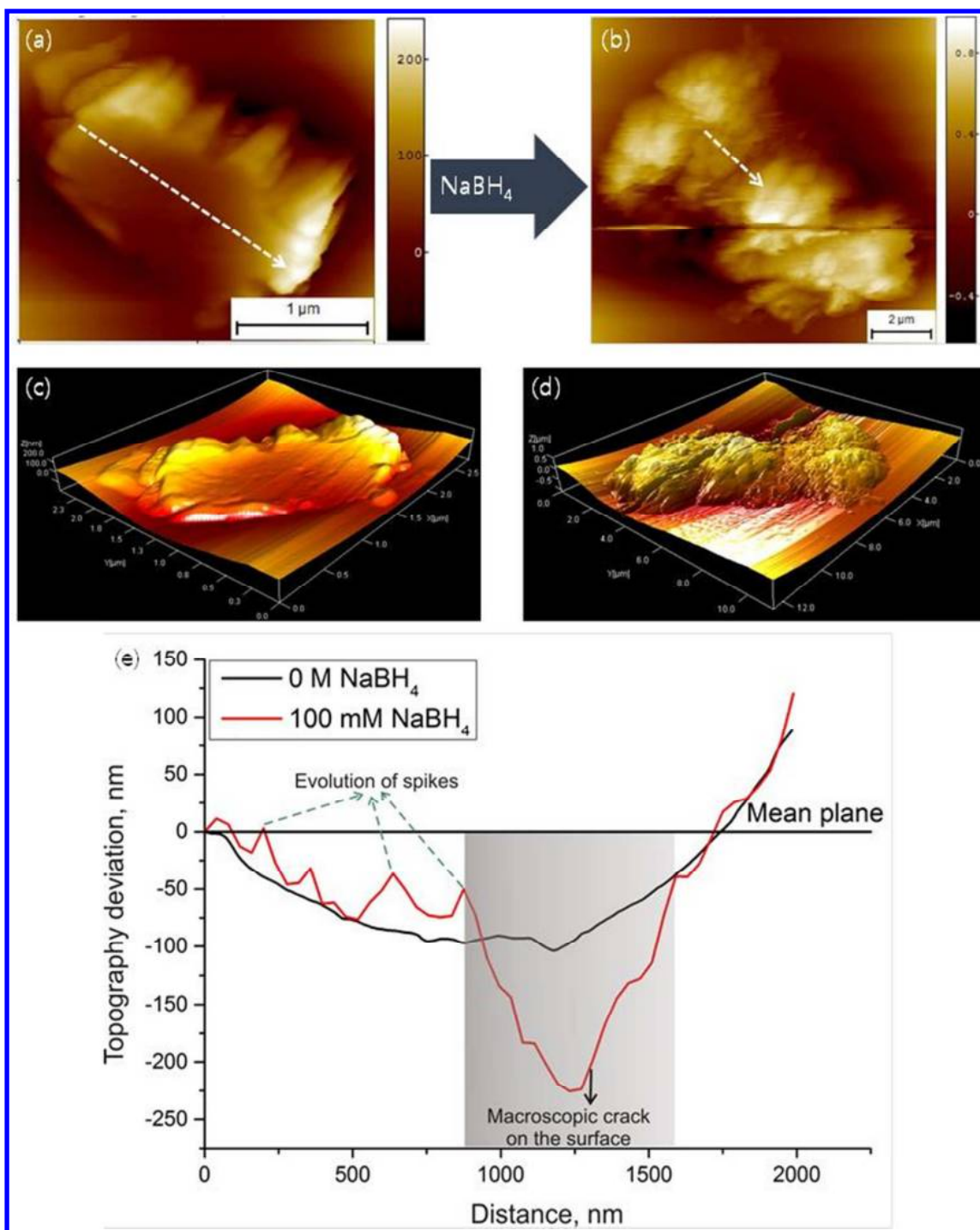


Figure 4

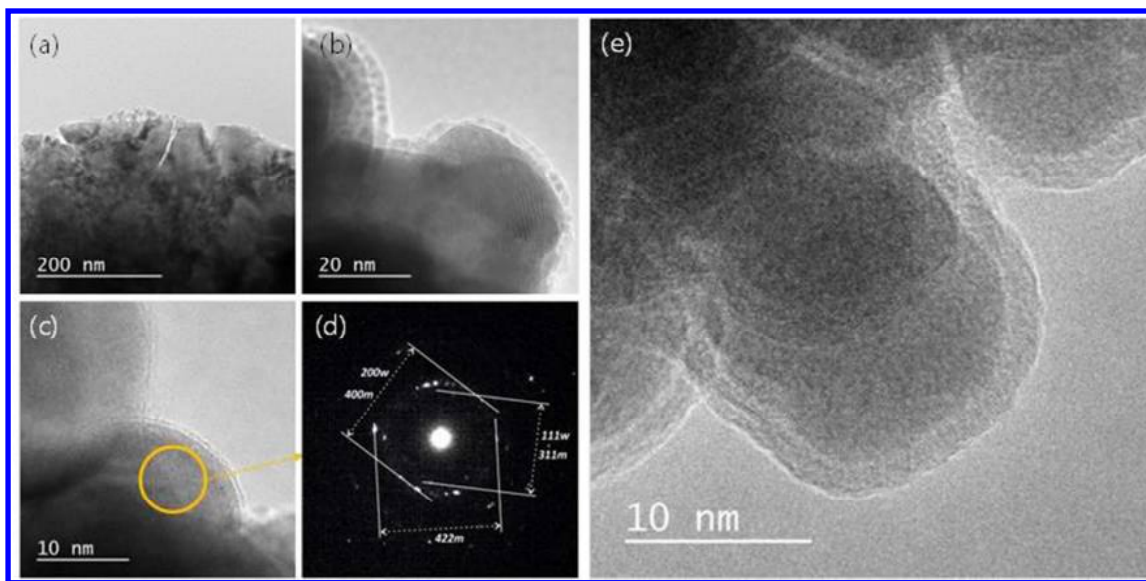


Figure 5

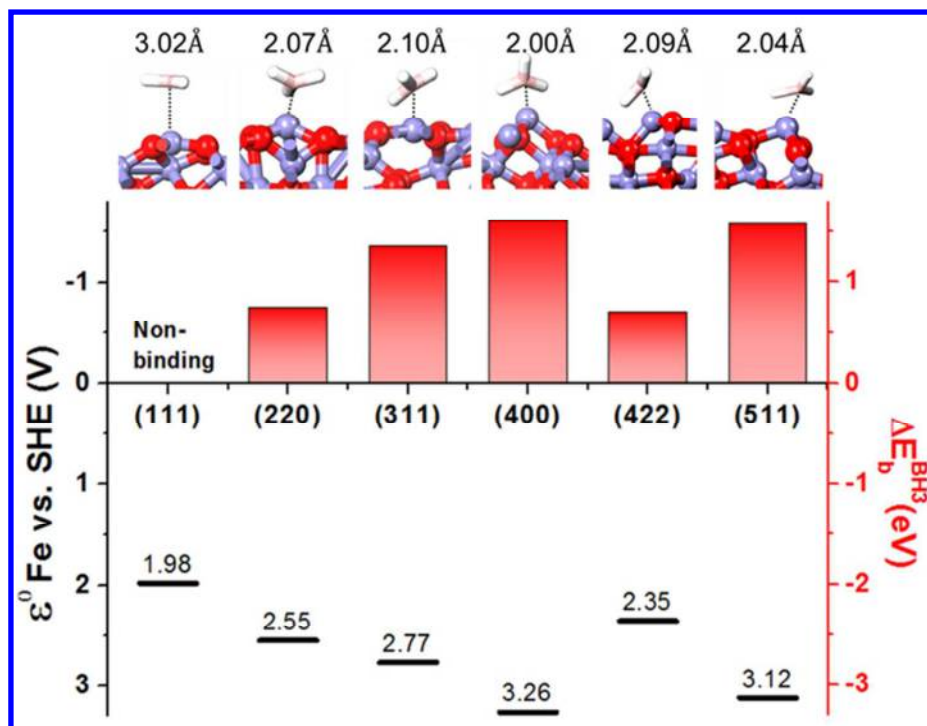


Figure 6

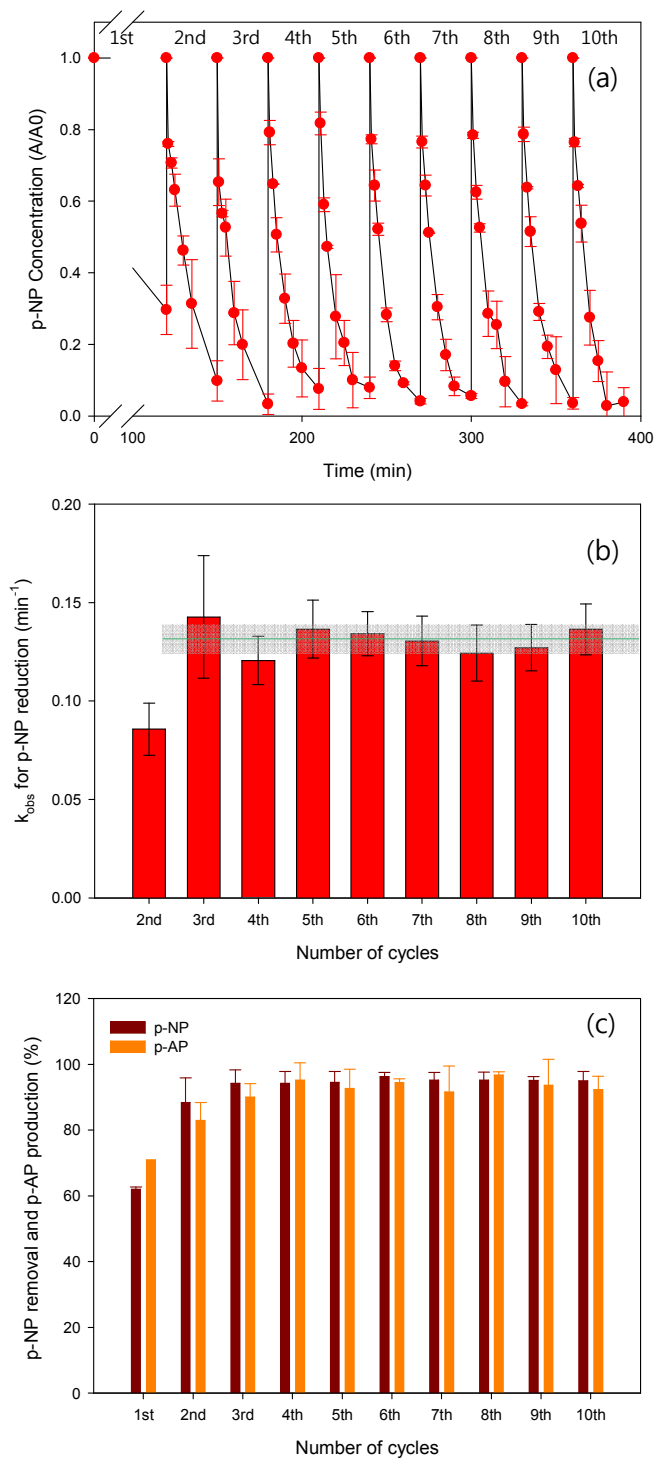


Figure 7

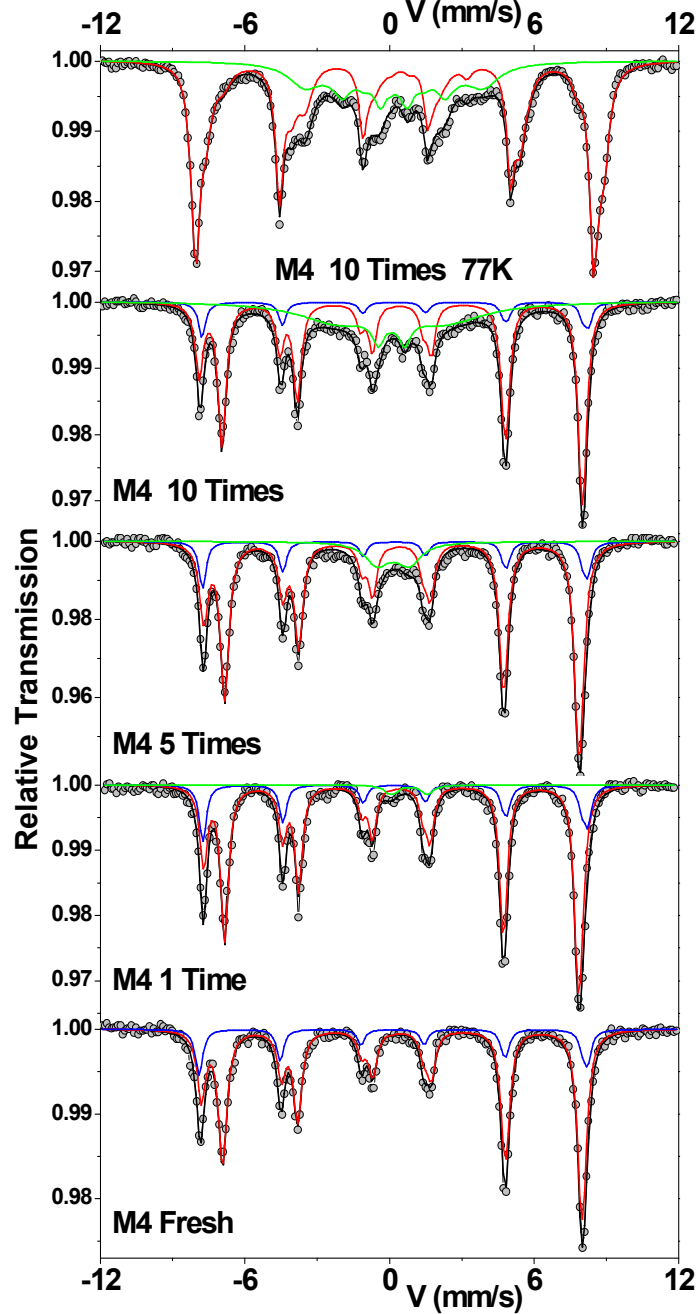


Figure 8

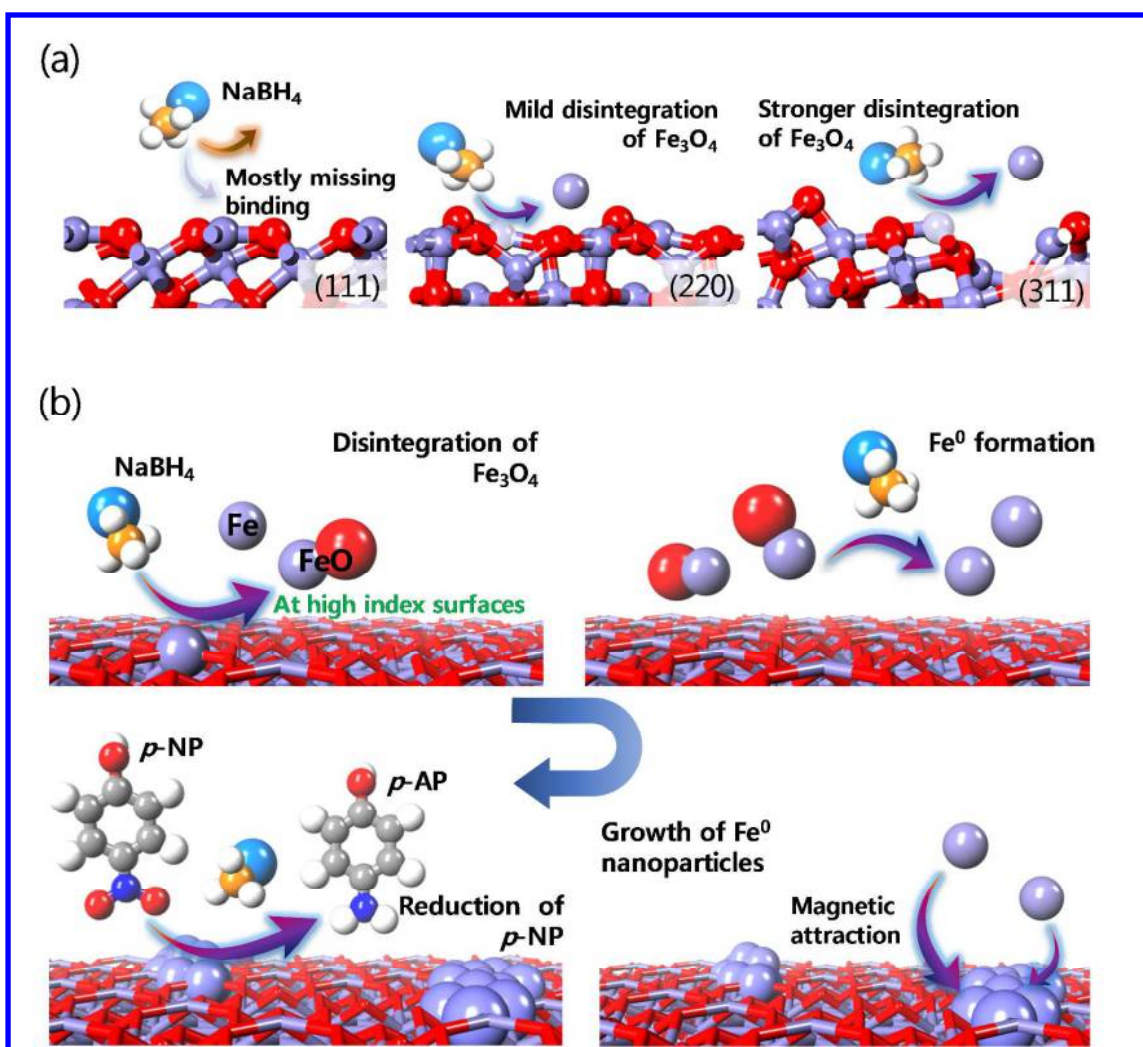


Figure 9

37
38
39
40
41
42
43
44
45
46
47
48
49
50
51
52
53
54
55
56
57
58
59
60

